Spin injection into silicon in three-terminal vertical and four-terminal lateral devices with Fe/Mg/MgO/Si tunnel junctions having an ultrathin Mg insertion layer

Shoichi Sato,[1] Ryosho Nakane,[1,2] Takato Hada,[1] and Masaaki Tanaka[1,3]

[1]*Department of Electrical Engineering and Information Systems, The University of Tokyo, 7-3-1 Hongo, Bunkyo-ku, Tokyo 113-8656, Japan*

[2]*Institute for Innovation in International Engineering Education, The University of Tokyo, 7-3-1 Hongo, Bunkyo-ku, Tokyo 113-8656, Japan*

[3]*Center for Spintronics Research Network, The University of Tokyo, 7-3-1 Hongo, Bunkyo-ku, Tokyo 113-8656, Japan*

(Received 20 April 2017; published 18 December 2017)

We demonstrate that the spin injection/extraction efficiency is enhanced by an ultrathin Mg insertion layer ($\leqslant$2 nm) in Fe/Mg/MgO/n^+-Si tunnel junctions. In diode-type vertical three-terminal devices fabricated on a Si substrate, we observe the narrower three-terminal Hanle (N-3TH) signals indicating true spin injection into Si and estimate the spin polarization in Si to be 16% when the thickness of the Mg insertion layer is 1 nm, whereas no N-3TH signal is observed without the Mg insertion. This means that the spin injection/extraction efficiency is enhanced by suppressing the formation of a magnetically dead layer at the Fe/MgO interface. We also observe clear spin transport signals, such as nonlocal Hanle signals and spin-valve signals, in a lateral four-terminal device with the same Fe/Mg/MgO/n^+-Si tunnel junctions fabricated on a Si-on-insulator substrate. It is found that both the intensity and linewidth of the spin signals are affected by the geometrical effects (device geometry and size). We have derived analytical functions taking into account the device structures, including channel thickness and electrode size, and estimated important parameters: spin lifetime and spin polarization. Our analytical functions explain the experimental results very well. Our study shows the importance of suppressing a magnetically dead layer and provides a unified understanding of spin injection/detection signals in different device geometries.

DOI: 10.1103/PhysRevB.96.235204

I. INTRODUCTION

Si-based spin transistors, which have a ferromagnetic source and drain and a Si channel, have generated much attention since they are very attractive for building blocks in next-generation integrated circuits [1–3]. Spin transistors can be used for nonvolatile memory and reconfigurable logic circuits because their transistor characteristics can be changed by the magnetization configuration of the ferromagnetic source and drain. To realize their functions, we need large magnetoresistance in the source-channel-drain transport, which requires (1) efficient spin injection and extraction of spin-polarized electrons into and from a Si channel (so-called spin injection/extraction) and (2) efficient transport of spin-polarized electrons via the Si channel (so-called spin-dependent transport). Recently, spin metal-oxide-semiconductor field-effect transistor (MOSFET) operation at room temperature was reported, but the magnetoresistance ratio γ_{MR} was very small (0.02–0.12%) [4,5]. If the spin injection/extraction efficiency is greatly enhanced and spin-dependent transport via a Si channel becomes coherent, much larger γ_{MR} will be obtained in spin MOSFET operation. Although spin injection/extraction and spin-dependent transport in Si channels have been studied already [4–11], the physics and detailed mechanism remain unclear. Moreover, it has been theoretically pointed out that the device geometry can affect the spin injection/extraction signals (hereafter "geometrical effect") [12–16], but this is not experimentally verified yet. Recently, we analyzed broader three-terminal Hanle (B-3TH) signals (which do *not* originate from *true* spin injection [17–21]) obtained by the three-terminal method [15,22] and proposed a model [21] (hereafter "dead-layer model") suggesting that the coherency of electron spins is reduced by a magnetically dead layer forming at a ferromagnetic metal/oxide interface. Note that the dead layer can be an ultrathin (one atomic layer or less) paramagnetic layer or paramagnetic interface states. Our dead layer model predicts that the spin injection/extraction efficiency will be enhanced if we can eliminate such a dead layer.

In this study, we show that the spin injection efficiency is enhanced in Fe/Mg/MgO/Si junctions by inserting an ultrathin Mg layer (thickness $t_{Mg} \leqslant 2$ nm) between the ferromagnetic Fe layer and the MgO tunnel barrier. This enhancement is attributed to the suppression of the magnetically dead layer at the Fe/MgO interface, which is verified by the shape of B-3TH signals and magnetization measurements. It is noteworthy that the Mg insertion between Fe and MgO is a well-known technique in magnetic tunnel junctions (MTJs) to suppress the formation of a dead layer and to improve the spin coherence of tunneling electrons [23]. In order to analyze spin injection/extraction signals correctly, we prepared two types of device structures with different geometries. One device structure is called the "vertical device" (shown in Fig. 1), which is a tunnel diode structure with a circular electrode patterned on a bulk Si substrate. This structure allows us to estimate accurate spin polarization and spin lifetime with the narrower three-terminal Hanle (N-3TH) signals because it is not necessary to take into account the geometrical effect. The other device structure is called the "lateral device" [shown in Fig. 5(a) below], which has a thin-body Si channel with four electrodes patterned on a Si-on-insulator (SOI) substrate. This structure allows us to prove the true spin injection in the Si channel by the four-terminal (nonlocal) measurements [24]. However, the geometrical effect must be taken into account in the analysis.

In Sec. II, we investigate how the Mg insertion affects spin injection/extraction in the vertical devices and unprocessed junction structures with various Mg-layer thicknesses (t_{Mg} = 0–2 nm). N-3TH and B-3TH signals observed in the vertical devices are changed depending on t_{Mg}. By analyzing the

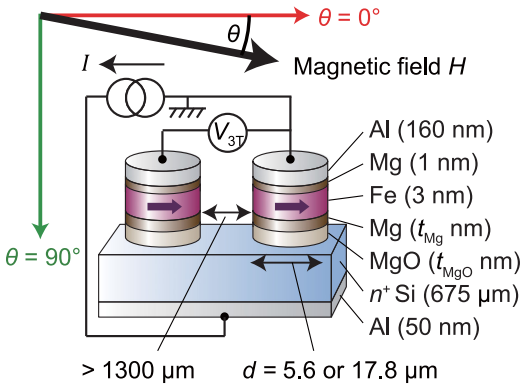

FIG. 1. Schematic illustration of the vertical device with Fe(3 nm)/Mg(t_{Mg}nm)/MgO(t_{MgO}nm)/n^+-Si tunnel junctions. The three-terminal measurement setup is also shown. Constant current I is driven from the top to the back, and three-terminal voltage V_{3T} is measured while an external magnetic field is applied (−3000–3000 Oe). The magnetic field direction angle θ is varied from 0° to 90°; $\theta = 0°$ and $\theta = 90°$ are the in-plane and normal-to-plane directions, respectively. The distance between the injection/extraction electrode and reference electrode is at least 1300 μm.

B-3TH signals using the dead-layer model, we find that the dead layer at the Fe/MgO interface is suppressed by the Mg insertion, leading to the true spin injection (extraction) into (from) Si. The suppression of the dead layer is supported by the magnetization measurements of the unprocessed samples. A relatively high spin polarization $P = 16\%$ in Si is obtained when the Mg-layer thickness is 1 nm.

In Sec. III, we verify the realization of spin transport and pure spin current in a Si channel using a lateral device with a 1-nm-thick Mg insertion layer. We observe four-terminal Hanle (4TH) signals, four-terminal spin-valve signals, and N-3TH signals in the lateral device. To analyze the experimental results, we derive analytical functions which take into account the effect of the channel thickness and the electrode lengths. By comparing the spin injection/extraction signals in the both vertical and lateral devices, we experimentally show that the geometrical effect must be taken into account for the precise analysis of spin injection/detection and spin transport.

II. Mg INSERTION IN THE VERTICAL DEVICES

A. Sample preparation

Figure 1 shows a schematic illustration of the vertical device with (from top to bottom) an Al(∼160 nm)/Mg(1 nm)/Fe(3 nm)/Mg(t_{Mg})/MgO(t_{MgO})/n^+-Si(001) junction and an Al back-side contact, where the Mg insertion layer thickness t_{Mg} is 0–2 nm and the MgO tunnel barrier thickness t_{MgO} is 0.5–1.2 nm. The fabrication process is as follows: First, a phosphorus-doped n^+-Si(8×10^{19} cm^{-3}) substrate with a H-terminated surface was thermally cleaned at 900 °C for 15 min in an ultrahigh-vacuum chamber (base pressure of $\sim3\times10^{-7}$ Pa). Then, an MgO layer was deposited on the surface by electron-beam evaporation at 30 °C at a rate of 0.003 nm/s. It is noteworthy that the MgO layer was not crystallized from reflective high-energy electron diffraction (RHEED) observation. Subsequently, without breaking vacuum the substrate was transferred into a molecular beam epitaxy chamber via a vacuum transfer chamber; then Mg/Fe/Mg multilayers and an Al (∼10 nm) cap layer were successively deposited at room temperature using Knudsen cells. Here, the bottom Mg layer (t_{Mg} nm) was inserted to prevent the reaction of the Fe layer and the MgO tunnel barrier and thereby to suppress the formation of a dead layer, and the top Mg layer (1 nm) was inserted to prevent the reaction of the Fe layer and the Al cap layer [25]. Then, immediately after being exposed to air, a 160-nm-thick Al layer was deposited on the surface, and top electrodes with diameter $d = 5.6$ and 17.8 μm were fabricated by UV lithography and H_3PO_4 etching for many junctions. Finally, an Al layer was deposited on the back of the substrate just after removing native oxide by Ar ion milling and HF etching. The junction area for I-V measurements was 25 μm^2($d = 5.6\,\mu$m), whereas that for spin injection/extraction measurements with the three-terminal method was 250 μm^2($d = 17.8\,\mu$m).

B. Magnetization of the nonprocessed sample

To measure the magnetic properties, a nonprocessed sample with the same layered structure with $t_{Mg} = 0$–2 nm and $t_{MgO} = 2$ nm was also prepared as a reference. Figure 2(a) shows t_{Mg} dependence of the saturation magnetization M_S, which was estimated from magnetization vs in-plane magnetic field (M-H) curves measured at 4 K by a superconducting quantum interference device magnetometer. Since M_S increases with increasing t_{Mg} and saturates at $t_{Mg} \geqslant 1$ nm, the

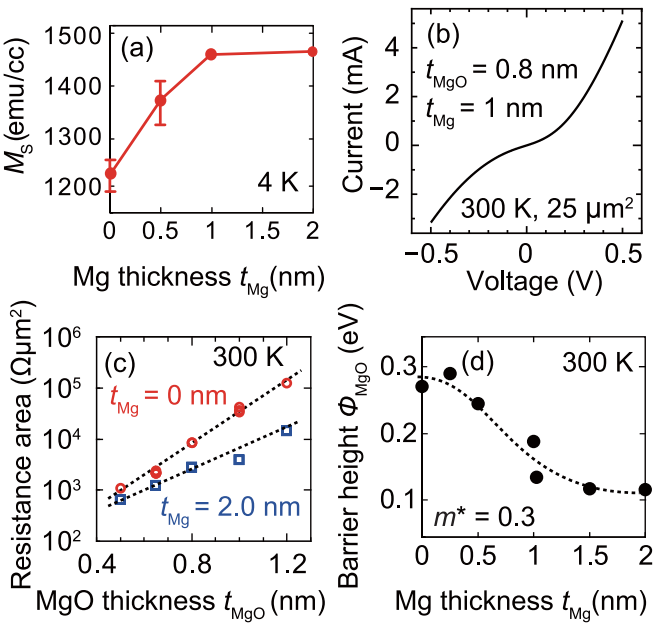

FIG. 2. (a) Saturation magnetization M_S of nonprocessed samples with the same layered structure as in Fig. 1 with various t_{Mg} (0, 0.5, 1.0, and 2.0 nm) and $t_{MgO} = 2$ nm, which were measured at 4 K with an in-plane magnetic field of 20–30 kOe. (b) I-V characteristic measured at 300 K of the vertical device with $t_{Mg} = 1$ nm and $t_{MgO} = 0.8$ nm. (c) Resistance area at $V = 0$ estimated from the I-V characteristics plotted as a function of t_{MgO}. From the dotted lines, the MgO barrier height Φ_{MgO} was estimated to be 0.27 eV for $t_{Mg} = 0$ nm and 0.11 eV for $t_{Mg} = 2.0$ nm. (d) Φ_{MgO} plotted as a function of t_{Mg}, in which the dotted curve is a guide for eyes.

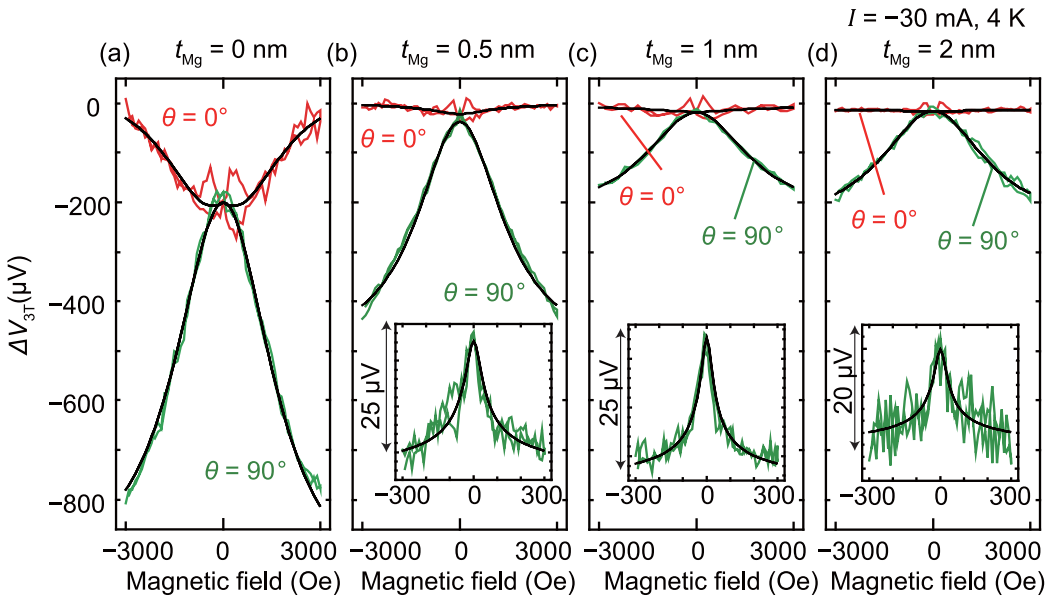

FIG. 3. Change in the three-terminal Hanle signals ΔV_{3T} measured at 4 K with $I = -30$ mA and in-plane magnetic field ($\theta = 0^\circ$) and normal-to-plane magnetic field ($\theta = 90^\circ$) for the sample with various Mg thicknesses: (a) $t_{Mg} = 0$ nm, (b) $t_{Mg} = 0.5$, (c) $t_{Mg} = 1.0$, and (d) $t_{Mg} = 2.0$ nm. Red and green curves represent the signals for the in-plane ($\theta = 0^\circ$) and the normal-to-plane ($\theta = 90^\circ$) magnetic field, respectively, and black solid curves are the fitting results using Eq. (1). Insets in (b)–(d) show the N-3TH signals in a lower field range (−300–300 Oe) after subtracting the B-3TH signals.

formation of a magnetically dead layer at the Fe/MgO interface was suppressed by the Mg insertion layer with $t_{Mg} \geqslant 1$ nm. Considering that $M_S = 1230\,\mathrm{emu/cm^3}$ at $t_{Mg} = 0$ nm and $M_S = 1450\,\mathrm{emu/cm^3}$ at $t_{Mg} = 2$ nm, the thickness of the dead layer at the Fe/MgO interface was estimated to be 0.3 nm when $t_{Mg} = 0$ nm. Since the dead layer is probably FeO_x [26], the constant M_S in $t_{Mg} \geqslant 1$ nm indicates that the Fe layer does not touch the bottom MgO layer; namely, the Mg layer fully covered the bottom MgO layer.

C. Experimental results of the *I-V* characteristics and three-terminal measurements

All the samples show nonlinear *I-V* curves as in Fig. 2(b) ($t_{MgO} = 0.8$ nm, $t_{Mg} = 1$ nm), and the resistance-area product at zero bias shows an exponential dependence on t_{MgO}, as shown in Fig. 2(c) ($t_{Mg} = 0$ and 2 nm). This indicates that tunnel current via the MgO barrier layer is dominant in our devices. From Simmons's equation [27] and Fig. 2(c), the barrier height of MgO Φ_{MgO} was estimated for each t_{Mg} and is plotted in Fig. 2(d); as t_{Mg} increases from 0 to 2 nm, $\Phi_{MgO}(=0.29\,\mathrm{eV})$ decreases at first and then becomes almost constant (0.11 eV) between 1 and 2 nm. Since the work functions of Fe and Mg are 4.7 and 3.7 eV [28], respectively, it is most likely that the barrier height is decreased by inserting the Mg layer between Fe and MgO. Combining the data of Figs. 2(a) and 2(d), the decrease in Φ_{MgO} results from the increase in the coverage of Mg over the MgO layer at $t_{Mg} < 1$ nm, and the constant Φ_{MgO} at $t_{Mg} \geqslant 1$ nm results from the full coverage of Mg over the MgO layer. As a consequence, the increase in M_S is correlated with the decrease in Φ_{MgO}, and $t_{Mg} = 1$ nm is the lowest thickness for obtaining the high M_S and the low Φ_{MgO} at the same time.

Figure 1 shows our three-terminal measurement setup, in which the junction voltage drop V_{3T} was measured by a voltmeter, while a constant current I was driven from the top electrode to the back of the substrate and an external magnetic field H was applied sweeping from −3000 to 3000 Oe along the in-plane ($\theta = 0^\circ$) or normal-to-plane ($\theta = 90^\circ$) direction. Note that the distance between the injection/extraction electrode and reference electrode is at least 1300 μm, which is much longer than the expected spin diffusion length (∼1 μm) [10]. Figures 3(a)–3(d) show the change in three-terminal signals $\Delta V_{3T}(H,\theta)$ of the samples with $t_{MgO} = 0.8$ nm and $t_{Mg} = 0$, 0.5, 1, and 2 nm, respectively, which were measured at 4 K with $I = -30$ mA (the spin extraction regime). In Figs. 3(a)–3(d), the red and green curves correspond to $\theta = 0^\circ$ and $\theta = 90^\circ$ conditions, respectively. B-3TH signals ($\theta = 90^\circ$) [17,21] and inverted three-terminal Hanle (I-3TH) signals ($\theta = 0^\circ$) [29] were observed at $H = -3000 - 3000$ Oe in all the samples, and their amplitudes decreased as t_{Mg} increased. Note that the N-3TH signals (*true* spin injection signal) [17,22] were observed at $H = -300 - 300$ Oe at $\theta = 90^\circ$ in the samples with $t_{Mg} \geqslant 0.5$ nm, as shown in the inset of Figs. 3(b)–3(d), whereas no N-3TH signal was observed in the sample with $t_{Mg} = 0$ nm.

It should also be noted that although N-3TH signals were observed in the spin *extraction* regime with $I = -30$ mA, as shown in the insets of Figs. 3(b)–3(d), no clear N-3TH signal was observed, and only B-3TH signals were observed in the spin *injection* regime with $I = +30$ mA (not shown here), as reported previously [30,31]. This difference in the N-3TH result due to the I polarity can be explained by the electric field in the Si channel at the MgO/Si interface [32]. In the spin extraction regime ($I < 0$), the electric field in the Si channel is almost screened by the accumulated electrons caused by the high n-type doping concentration $8 \times 10^{19}\,\mathrm{cm^{-3}}$

in Si [33]; namely, the electrical potential in Si is almost flat. Thus, the electron spins in Si are purely diffusive in the spin extraction regime. On the other hand, in the spin injection regime ($I > 0$), a depletion layer is formed in Si near the MgO/Si interface, and the electron spins injected into Si drift away from the interface by the electric field in the depletion layer. Using the one-dimensional (1D) Poisson's equation, the maximum electric field strength in the Si depletion layer in our sample was estimated to be 3.4 MV/cm when $I = +30$ mA, and this electric field decreases the amplitude of the N-3TH signal down to ∼14% and broadens the linewidth by ∼3000%, compared with those in the spin extraction regime [see Supplemental Material (SM) [34]]. Thus, it is reasonable that no clear N-3TH signal appears in the spin injection regime, probably because such weak and broadened N-3TH signals cannot be distinguished from the intense B-3TH signals even if they exist. So far, the disappearance of spin injection signals in three-terminal devices with a Si channel has been reported [30,31], but the reason has not been clarified. This is probably because the spin injection/extraction signals were analyzed using the simple 1D spin diffusion equation which was established in all metallic systems; that is, semiconducting properties of the Si channel have not been taken into account in the analysis so far. As we suggest here, the electric field and the depletion layer differ in the Si channel between the injection and extraction conditions, even if the doping concentration of Si is significantly high. Thus, this electric field effect is important to design semiconductor-based spintronic devices using spin injection and detection.

D. Analysis of the three-terminal signals

Considering that the three-terminal signals $\Delta V_{3T}(H,\theta)$ are the superposition of the N-3TH signal $\Delta V^{\text{N-3TH}}(H,\theta)$ and the B-3TH signal $\Delta V^{\text{B-3TH}}(H,\theta)$, we analyzed the signals in Figs. 3(a)–3(d) with the equation $\Delta V_{3T}(H,\theta) = \Delta V^{\text{N-3TH}}(H,\theta) + \Delta V^{\text{B-3TH}}(H,\theta)$, as the same procedure in our previous study [21]. Since the electrode diameter ($d = 17.8\,\mu$m) is much larger than the expected spin diffusion length ($\lambda_S \sim 1\,\mu$m) [10] and the electric field in Si is negligible in the spin extraction regime, as mentioned earlier, the 1D spin diffusion model is applicable. The B-3TH and N-3TH functions for the vertical device ($\Delta V^{\text{N-3TH(vertical)}}$) are as follows [17,21,22,35] (see SM for details [34]):

$$\Delta V^{\text{B-3TH}}(H,\theta) = \eta_{\text{B-3TH}} V_0 \frac{(H\cos\theta+S)^2+C^2}{(H\cos\theta+S)^2+(H\sin\theta)^2+B^2+C^2}, \quad (1)$$

$$\Delta V^{\text{N-3TH(vertical)}}(H,\theta) = \Delta V_0^{\text{spin}} \left[\sqrt{\frac{1+\sqrt{1+(\gamma H\tau_S)^2}}{2+2(\gamma H\tau_S)^2}} \sin^2\theta + \cos^2\theta \right], \quad (2)$$

$$\Delta V_0^{\text{spin}} = J\rho\lambda_S P^I P^D, \quad (3)$$

where J is the current density, P^I is the spin polarization of electrons injected into Si (hereafter "injection polarization"), P^D is the spin polarization detected by the detection electrode (hereafter "detection polarization"), H is the external applied field, θ is the field angle, γ is the gyromagnetic ratio, τ_S is the spin lifetime in Si, λ_S is the spin diffusion length, ρ is the Si resistivity, V_0 is the offset voltage drop of the tunnel junction at $H = 0$, and $\eta_{\text{B-3TH}}$ is the B-3TH ratio [21]. Ideally, when spin injection/extraction efficiency is 100%, P^I and P^D are the same as the spin polarization of the Fe electrode (∼40%) [36]. Parameters C, B, and S in Eq. (1) are the effective internal magnetic fields in the ultrathin magnetically dead layer introduced in our previous study (see SM of Ref. [21]). S is the directional field parallel ($S > 0$) or antiparallel ($S < 0$) to the magnetization M_{Fe} of the Fe layer, C is the nondirectional field parallel to M_{Fe}, and B is the nondirectional field perpendicular to M_{Fe}. Parameter B is the primary indicator of a magnetically dead layer and is strongly related to the I-3TH signal. As B decreases, the amplitude of the I-3TH signal decreases. When the paramagnetic state completely vanishes and ferromagnetic order appears in a magnetically dead layer, the I-3TH signal disappears, and $B = 0$. In the analysis, we use $\gamma = 1.76\times10^7\ \text{s}^{-1}\ \text{Oe}^{-1}$ and assume that the spin injection and detection polarizations are the same value, P_{3T}; that is, $P_{3T} = P^I = P^D$. It is notable that Eq. (2) is twice as large as the conventional N-3TH functions [9]. This is because injected spins diffuse vertically down to the back of the substrate in this device structure, whereas they diffuse laterally to both the left and right sides in the lateral devices on a SOI substrate (see SM [34]).

First, the B-3TH signals were analyzed since these must be subtracted from $\Delta V_{3T}(H,\theta)$ to extract and analyze the N-3TH signals. Black solid curves in Figs. 3(a)–3(d) are fitting results using Eq. (1). By fitting Eq. (1) to the experimental results in Figs. 3(a)–3(d), B, C, S, and $\eta_{\text{B-3TH}}$ were estimated and are plotted in Figs. 4(a) and 4(b). It was found that S and C increase and B decreases as t_{Mg} increases, and this means that the magnetically dead layer thickness is decreased and ferromagnetic order is increased at the Fe/Mg/MgO interface with increasing t_{Mg} [21]. Considering this result along with the fact that S is positive except at $t_{Mg} = 0$ nm, the ferromagnetic order appeared, and the formation of the dead layer was suppressed at $t_{Mg} \geqslant 0.5$ nm. This is consistent with the result that the N-3TH signals were observed only at $t_{Mg} \geqslant 0.5$ nm [see the insets of Figs. 3(b)–3(d)]. Also, as shown in Fig. 4(b), $\eta_{\text{B-3TH}}$, which is the ratio of the amplitude of B-3TH and I-3TH signals to the tunnel voltage drop, also decreased with increasing t_{Mg}. Thus, B, C, S, and $\eta_{\text{B-3TH}}$ are correlated with each other, and they are also correlated with M_S in Fig. 2(a), as expected.

Then, the N-3TH signals in the insets of Figs. 3(b)–3(d) were analyzed by fitting Eqs. (2) and (3) to the experimental signals with the measurement parameters $J = 0.12\,\text{A}/\mu\text{m}^2$, $\rho = 1.0\,\text{m}\Omega\,\text{cm}$, and $\lambda_S = 1\,\mu$m taken from Ref. [10]. Black solid curves in the insets of Figs. 3(b)–3(d) are fitting results. Figures 4(c) and 4(d) show the estimated τ_S and P_{3T}, respectively. The spin lifetime obtained by fitting was almost constant ($\tau_S \sim 2$ ns) for all t_{Mg}, which is reasonable because τ_S depends only on the Si substrate property and is independent of the junction properties. Moreover, this τ_S value of ∼2 ns is consistent with the previously reported values (1–10 ns) [8,10,37,38] and is in good agreement with the theoretically calculated value (2.5 ns) for the same phosphorus

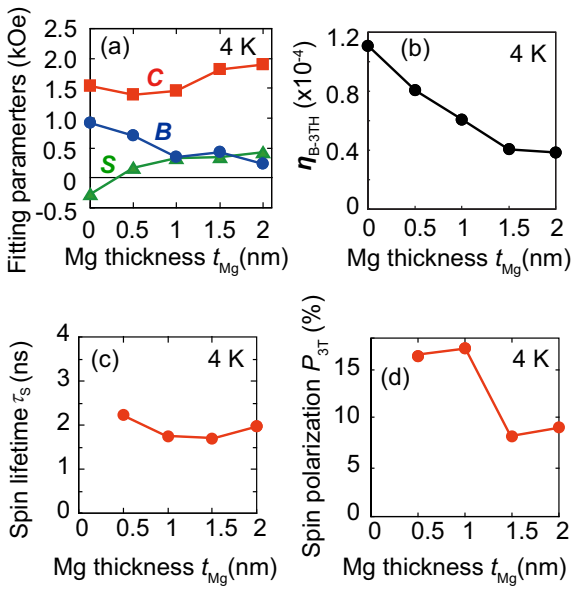

FIG. 4. Mg thickness t_{Mg} dependence of the fitting parameters (a) B, C, and S and (b) $\eta_{B\text{-}3TH}$ estimated using Eq. (1) and the experimental B-3TH and I-3TH signals in Figs. 3(a)–3(d). Blue circles, red squares, and green triangles in (a) represent the values for B, C, and S, respectively. The t_{Mg} dependence of the fitting parameters (c) τ_S and (d) P_{3T} ($= P^I = P^D$ was assumed) estimated using Eqs. (2) and (3) and the N-3TH signals in the insets of Figs. 3(b)–3(d).

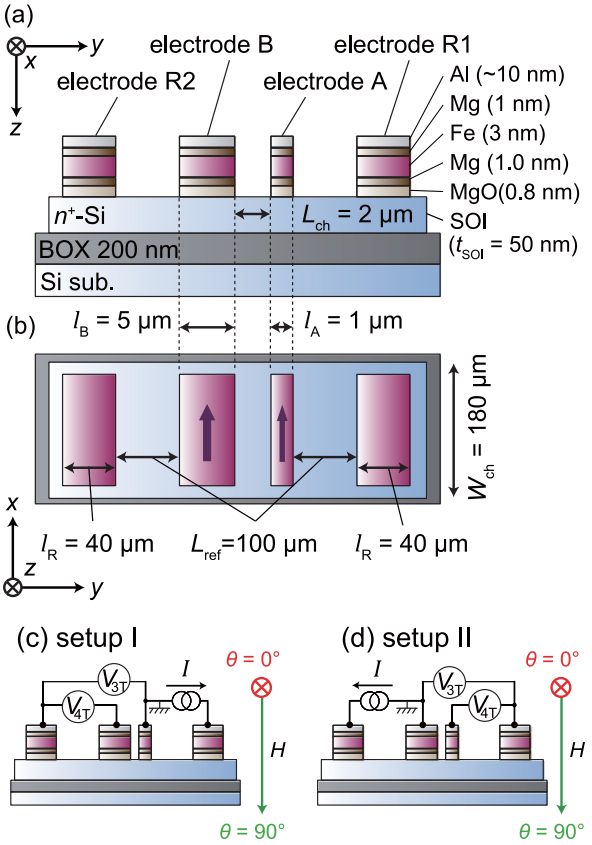

FIG. 5. (a) Side view and (b) top view of the lateral device with Fe(3 nm)/Mg(1 nm)/MgO(0.8 nm)/n^+-Si tunnel junctions fabricated on a silicon-on-insulator (SOI) substrate for four-terminal measurements. Four electrodes are labeled R2, B, A, and R1 from the left to right. Coordinates are defined as follows; x and y are parallel to the long and short sides of the electrodes, respectively, and z is normal to the substrate plane. Four-terminal measurement (c) setup I and (d) setup II, where the three-terminal signal V_{3T} and four-terminal signal V_{4T} are measured at the same time while an external magnetic field is applied (−3000–3000 Oe). The magnetic field direction angle θ is varied from 0° to 90°; $\theta = 0^\circ$ and $\theta = 90^\circ$ are the in-plane and normal-to-plane directions, respectively.

concentration in Si [39]. On the other hand, $P_{3T} = 8$–16% in Fig. 4(d) is comparable to the previously reported values of 5–17% [10–11]. In contrast to τ_S, P_{3T} changes depending on t_{Mg}; $P_{3T} \sim 16\%$ for $t_{Mg} = 0.5$ and 1.0 nm, and $P_{3T} \sim 8\%$ for $t_{Mg} = 1.5$ and 2.0 nm. Although the dead-layer formation was significantly suppressed when $t_{Mg} \geqslant 1.0$ nm, the injected electron spins lost their polarization while passing through the Mg layer when $t_{Mg} \geqslant 1.5$ nm. Thus, we conclude that $t_{Mg} = 1.0$ nm is the best condition for our spin injection/detection junctions.

III. SPIN-DEPENDENT TRANSORT IN THE LATERAL DEVICE

A. Sample preparation

To confirm the spin injection into the Si layer and the spin transport in the Si channel and also to explore the geometrical effect [12–16] on spin-related signals, a lateral device structure was fabricated on an SOI substrate, as shown in Figs. 5(a) and 5(b), and the spin transport properties are compared with those of the vertical devices in Fig. 1. Figures 5(a) and 5(b) are schematic side-view and top-view illustrations, respectively, of the lateral device with the same junction structure as that in the vertical device in Fig. 1(a) with $t_{Mg} = 1.0$ nm and $t_{MgO} = 0.8$ nm. The fabrication process is as follows: First, an undoped SOI substrate was doped with phosphorus using the thermal diffusion method with a P_2O_5 film on the surface. Using secondary-ion-mass spectroscopy, we confirmed a uniform phosphorus doping concentration of $\sim 10^{20}$ cm^{-3} in the Si channel layer (this means that the doping profiles in our vertical and lateral devices are very similar). After removing the P_2O_5 film and successive cleaning with H_2SO_4 solution, a H-terminated surface was formed with HF. Then, tunnel junctions were formed by the same procedure as that for the vertical device. After being exposed to air, a 100-nm-thick Ta layer was deposited on the surface, and electrodes were formed by electron-beam lithography and Ar ion milling. Finally, each device was isolated by etching the Si body layer with CF_4 gas, as shown in Figs. 5(a) and 5(b). The channel length L_{ch} and width W_{ch} are 2 and 180 μm, respectively, and the lengths l_A and l_B along the y direction of electrode A and electrode B (the inside two electrodes) are 1 and 5 μm, respectively. The outside electrodes R1 and R2 with $l_R = 40$ μm in length along the y direction are the reference electrodes, and the distance L_{ref} between electrodes A and R1 (B and R2) is $\sim$100 μm. Since the Si channel resistivity is $\sim$1 mΩ cm from the I-V characteristics, the electron carrier density is estimated to be $\sim 1 \times 10^{20}$ cm^{-3}. Thus, $L_{ref} = 100$ μm is much longer than the expected spin diffusion length of $\sim$1 μm in Si with

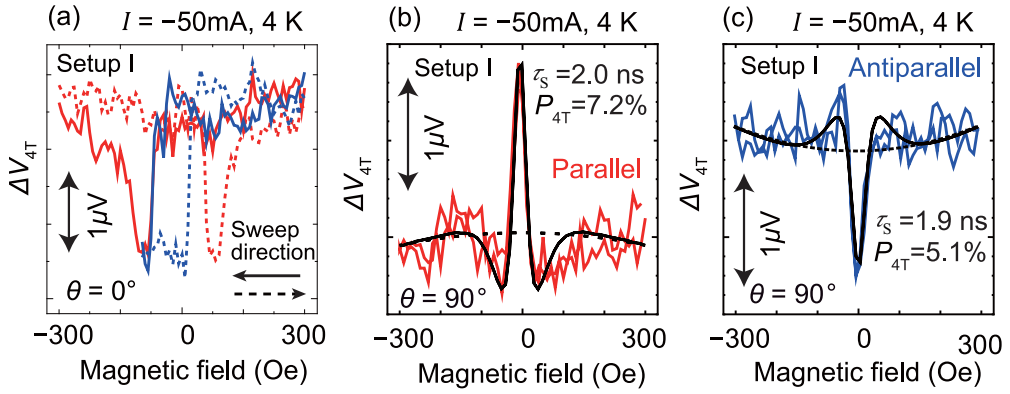

FIG. 6. (a) Change in the four-terminal signal ΔV_{4T} as a function of in-plane magnetic field ($\theta = 0^\circ$), indicating the spin-valve effect, measured at 4 K with $I = -50$ mA in setup I. Red solid and dashed and blue solid and dashed curves are major and minor loops, respectively. Four-terminal Hanle signals ΔV_{4T} as a function of normal-to-plane magnetic field ($\theta = 90^\circ$) measured at 4 K with $I = -50$ mA in the (b) parallel and (c) antiparallel magnetization configurations. Black solid and black dashed curves are the fitting results with Eq. (4) and parabolic backgrounds, respectively.

this doping concentration [10]. Figures 5(c) and 5(d) show our four-terminal measurement setups I and II, respectively. Here, in setup I, we define the four-terminal voltage V_{4T} and three-terminal voltage V_{3T} as follows: V_{4T} is the voltage between electrodes B and R2, and V_{3T} is the voltage between A and R2. We measure V_{3T} and V_{4T} while a constant current ($I = \pm 50$ mA) is driven from electrode A to R1 and an external magnetic field is applied sweeping between -3000 and $+3000$ Oe along the in-plane (the x axis, $\theta = 0^\circ$) or normal-to-plane (the z axis, $\theta = 90^\circ$) direction. V_{4T} and V_{3T} in setup II are also defined by exchanging connection A with B and R1 with R2.

B. Experimental results of four-terminal measurements

Figure 6(a) shows the change ΔV_{4T} in V_{4T} measured in setup I with an in-plane magnetic field ($\theta = 0^\circ$) and $I = -50$ mA (the spin extraction regime), where the red and blue curves represent the major and minor loops, respectively. Since the major loop of ΔV_{4T} shows two minimum plateaus between 50 and 80 and -50 and -80 Oe, which reasonably agree with the coercivities of electrodes A and B, this is the spin-valve signal. Figures 6(b) and 6(c) show ΔV_{4T} signals in the parallel and antiparallel magnetization configurations measured in setup I with a normal-to-plane magnetic field ($\theta = 90^\circ$) and $I = -50$ mA, where the red and blue curves represent the signals measured in the parallel and antiparallel magnetization configurations, respectively. Almost the same signals as in Figs. 6(a)–6(c) with inverted polarity are observed with $I = 50$ mA (spin injection regime, not shown). Clear Hanle signals with the change in polarity depending on the magnetization configuration give strong evidence that spin-polarized electrons are transported via the Si channel [24]. Moreover, the amplitude of the signal change of ~ 2 μV in Fig. 6(a) is nearly equal to the sum of the signal changes observed in Figs. 6(b) and 6(c), indicating that the data in Fig. 6(a) are caused by the spin-valve effect.

On the other hand, the red curves in Figs. 7(a) and the blue curves in Fig. 7(b) are ΔV_{3T} at $\theta = 0^\circ$ measured in setup I and setup II, respectively. In addition, the red and blue curves in Fig. 7(c) are the same signals between -300 and $+300$ Oe in Figs. 7(a) and 7(b), respectively. The hysteresis characteristics of these signals probably come from the tunnel anisotropic magnetoresistance (TAMR) [40] since the signals in setups I and II show the minimum values at the coercivities of electrode A (± 80 Oe) and electrode B (± 50 Oe), respectively. We considered that the ΔV_{3T} signal at $\theta = 0^\circ$ is composed of both this hysteretic TAMR signal and the I-3TH signal and fitted Eq. (1) to estimate the I-3TH signal, as illustrated by the black curve in Figs. 7(a) and 7(b). As in the case of the vertical device, the amplitude of the I-3TH signal was small compared with the B-3TH signal, which confirms the suppression of the dead layer at the Fe/Mg/MgO interface of electrodes A and B by inserting an ultrathin Mg layer between the Fe and MgO layers.

We also show ΔV_{3T} signals measured with a normal-to-plane magnetic field ($\theta = 90^\circ$) in setups I and II by the green and light brown curves in Figs. 7(a) and 7(b), respectively, where the fitting results of the B-3TH signals using Eq. (1) are also shown by the black solid curves (details are given later). Comparing the ΔV_{3T} signals in the vertical [Fig. 3(c)] and lateral [Figs. 7(a) and 7(b)] devices with the same t_{Mg} and t_{MgO}, the amplitude of the N-3TH and the TAMR signals in the lateral device is several times larger than that in the vertical devices (details are given later), while the amplitudes of the B-3TH and I-3TH signals in both devices are almost the same. The same amplitude of the B-3-TH and I-3TH signals in the two types of device structures confirms again that the B-3TH and I-3TH signals do not originate from spin accumulation in the Si channel but from the magnetoresistance depending on the tunnel junction properties [17–21,38]. If we use the function (2) which was derived from the 1D spin diffusion model, the larger N-3TH signals observed in the lateral device lead to inconsistent fitting results $P_{3T} = 20\%$ and $\tau_S = 1.0$ ns (electrode A) and $P_{3T} = 63\%$ and $\tau_S = 2.3$ ns (electrode B), although P_{3T} and τ_S should be comparable in both electrodes and also to those in the vertical device with $t_{Mg} = 1$ nm ($P_{3T} = 16\%$ and $\tau_S = 1.7$ ns). This means that spin accumulation signals in the lateral device must be analyzed by a more sophisticated model taking into account the geometrical effects when the geometrical scale of the structure, such as the SOI channel thickness and electrode

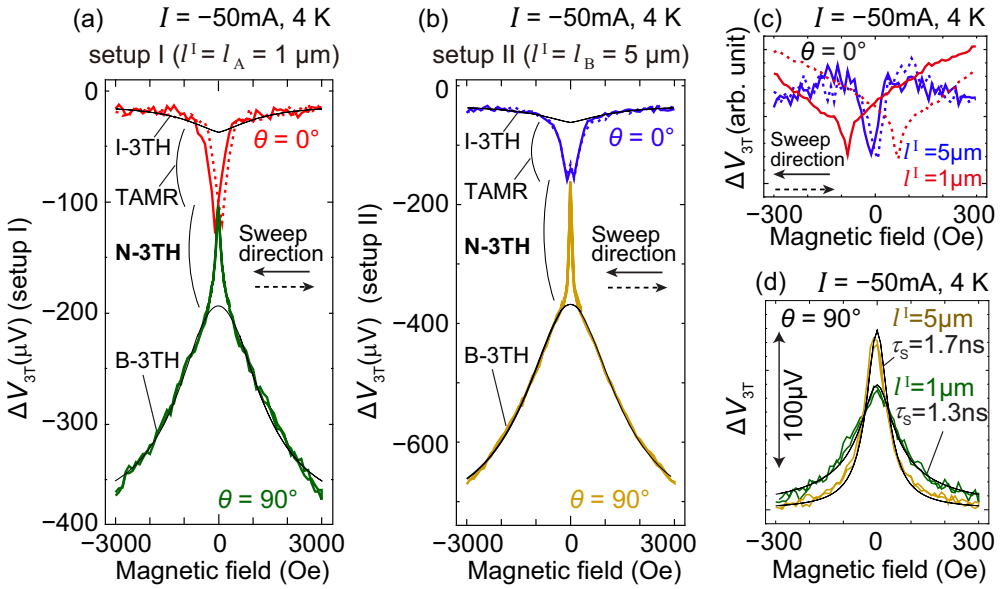

FIG. 7. Change in the three-terminal signals ΔV_{3T} measured at 4 K with $I = -50$ mA in (a) setup I and (b) setup II, where red and blue curves represent the signals for the in-plane magnetic field ($\theta = 0^\circ$) and green and light brown curves represent the signals for the normal-to-plane magnetic field ($\theta = 90^\circ$). Fitting curves of the I-3TH and the B-3TH signals with Eq. (1) are also shown by black solid curves. (c) ΔV_{3T} signals ($\theta = 0^\circ$) within ±300 Oe, where solid and dotted red curves and solid and dotted blue curves are the signals in (a) and (b), respectively. (d) Normal-to-plane N-3TH signals ($\theta = 90^\circ$) after subtracting B-3TH within ±300 Oe, where green and light brown curves are the experimental curves in (a) and (b), respectively. Black solid curves are fitting results with Eq. (5).

length, is smaller than λ_S. The geometrical effects on the spin accumulation signals were pointed out by other groups [12–16] but have never been experimentally verified. In this study, we use two device structures with different geometries, and thus, we can clarify what determines the shape and amplitude of the N-3TH signal by comparing the N-3TH signals in these two device structures. On the contrary, the difference in the TAMR signals in the vertical and lateral devices probably reflects the magnetization switching process of the Fe electrodes in each device because the shape of the Fe electrodes in each device is different. It is reported that the TAMR signal is proportional to both the tunnel resistance and the vertical component of the magnetization vector [40]. Considering that the tunnel area resistance is about 10 kΩ μm^2 and the amplitude of the TAMR in the lateral device [Figs. 7(a) and 7(b)] is 0.5−2 Ω μm^2, the difference in the TAMR signals in the vertical and lateral devices can occur when the vertical component of the Fe magnetization changes by ∼0.02% during the magnetization switching process. Such a change in the Fe magnetization switching process is possible because it is strongly affected by the shape of the ferromagnets.

C. Analysis of the four-terminal signals

Based on the two-dimensional (2D) spin diffusion model and the ideas in Refs. [12–14], we originally constructed the following analytic functions for ΔV_{3T} and ΔV_{4T} in the lateral device ($\Delta V^{\text{N-3TH(lateral)}}$ and $\Delta V^{\text{4TH(lateral)}}$) while taking into account the injector electrode length l^I, detector electrode length l^D, and the SOI thickness t_{SOI} (see SM for a detailed derivation [34]):

$$\Delta V^{\text{4TH(lateral)}}(H,\theta = 90^\circ) = \Delta V_0^{\text{spin}} \frac{1}{2}\frac{\lambda_S}{t_{SOI}} \text{Re}\left[\frac{1}{1+i\gamma H\tau_S}\exp(-\alpha L_{ch})\frac{1}{\alpha l^D}[1-\exp(-\alpha l^D)][1-\exp(-\alpha l^I)]\right] \quad (4)$$

for ΔV_{4T}, and

$$\Delta V^{\text{3TH(lateral)}}(H,\theta = 90^\circ) = \Delta V_0^{\text{spin}} \frac{\lambda_S}{t_{SOI}} \text{Re}\left[\frac{1}{1+i\gamma H\tau_S}\left\{1-\frac{1}{\alpha l^I}[1-\exp(-\alpha l^I)]\right\}\right] \quad (5)$$

for ΔV_{3T},where $\alpha = \frac{\sqrt{1+i\gamma H\tau_S}}{\lambda_S}$, i is the imaginary unit, and Re[·] is the real part of the square brackets. In deriving Eqs. (4) and (5), we assume that the spin injection (current density) is uniform over the electrode, $t_{SOI} \ll \lambda_S$, and $W_{ch} \gg \lambda_S$. Here, the factor λ_S/t_{SOI} in Eqs. (4) and (5) is an indicator of the channel confinement effect (CCE), which means that the spin accumulation is significantly larger than that in the vertical device as t_{SOI} becomes smaller than λ_S [12]. Also, the factors $\frac{1}{\alpha l^D}[1-\exp(-\alpha l^D)][1-\exp(-\alpha l^I)]$ in Eq. (4) and $\frac{1}{\alpha l^I}[1-\exp(-\alpha l^I)]$ in Eq. (5) are indicators of the electrode averaging effect (EAE), which means averaging the spin detection signals over the detector along the y direction. As l^I

TABLE I. P_{3T}, P_{4T}, and τ_S estimated from the experimental signals with $I = -50$ mA (spin extraction regime) in Figs. 3(c), 6(b), and 7(d), using Eqs. (2)–(5) under various conditions: (i) Eqs. (4) and (5) (both CCE and EAE are taken into account), (ii) Eqs. (4) and (5) with $l^I, l^D \to 0$ (without EAE), and (iii) Eqs. (4) and (5) with $\lambda_S/t_{SOI} = 1$ and $l^I, l^D \to 0$ (without CCE and EAE). ND (not detected) denotes the absence of clear signal.

	Vertical device, N-3TH		Lateral device							
			N-3TH (setup I)		N-3TH (setup II)		4TH (setup I)		4TH (setup II)	
Condition	P_{3T} (%)	τ_S (ns)	P_{3T} (%)	τ_S (ns)	P_{3T} (%)	τ_S (ns)	P_{4T} (%)	τ_S (ns)	P_{4T}	τ_S
(i)	16	1.7	6.6	1.3	12	1.7	7.2	2.0	ND	ND
(ii)	16	1.7	4.5	1.0	14	2.3	2.5	2.1	ND	ND
(iii)	16	1.7	20	1.0	63	2.3	11	2.1	ND	ND

and l^D become longer, amplitudes and linewidths of N-3TH and 4TH signals are changed as follows: (1) Amplitudes of N-3TH signals become larger because CCE is more pronounced. (2) Amplitudes of 4TH signals become smaller because the maximum distance between the injector and detector electrodes becomes longer. (3) Linewidths of both the N-3TH and 4TH signals become narrower. This means that the injected spins are dephased by a smaller magnetic field because the phase variation of the detected spins becomes larger.

In setup I, $l^I = l_A$ and $l^D = l_B$ are used, and in setup II, $l^I = l_B$ and $l^D = l_A$ are used. From the fitting, τ_S, λ_S, and the average spin polarization $P_{4T} = \sqrt{P^I P^D}$ are estimated from Eqs. (3) and (4), and P_{3T} and τ_S of electrodes A($P_{3T(A)}$) and B($P_{3T(B)}$) are estimated from Eqs. (3) and (5).

In Figs. 6(b) and 6(c), the fitting results using Eq. (4) and parabolic backgrounds are shown by the black solid and dashed curves, respectively, from which $P_{4T} = 7.2\%$, $\tau_S = 2.0$ ns, and $\lambda_S = 1.0\,\mu$m were estimated. From the analysis of ΔV_{3T}, the B-3TH and I-3TH signals were analyzed using Eq. (1), and then the N-3TH signals were analyzed using Eq. (5). The black curves in Figs. 7(a) and 7(b) show the fitting results for the B-3TH and I-3TH signals, in which $S \sim 350$ Oe, $B \sim 450$ Oe, and $C \sim 1300$ Oe estimated using Eq. (1) are in good agreement with those estimated in the vertical device with $t_{Mg} = 1$ nm [see Fig. 4(a)]. To see the effect of EAE on the shape of N-3TH signals, the N-3TH signals obtained in electrode A (setup I, $l^I = l_A = 1\,\mu$m) and electrode B (setup II, $l^I = l_B = 5\,\mu$m) are shown in Fig. 7(d), where the green and light brown curves represent the signals obtained in electrodes A and B, respectively. The linewidths of the N-3TH signals in Fig. 7(d) are quite different between the two cases, but fitting with Eq. (5) (black curves) leads to comparable values: $\tau_S = 1.3$ ns for electrode A and 1.7 ns for electrode B. Furthermore, using $\lambda_S = 1.0\,\mu$m estimated from the 4TH signal [Fig. 6(b)], $P_{3T(A)} = 6.6\%$ and $P_{3T(B)} = 12\%$ are estimated from the N-3TH signals [Fig. 7(d)]. As a consequence, the parameters estimated from the N-3TH signals ($\sqrt{P_{3T(A)} P_{3T(B)}} = 9.1\%$ and $\tau_S = 1.3$–1.7 ns) are comparable to those from the 4TH signals ($P_{4T} = 7.2\%$ and $\tau_S = 2.0$ ns). This result confirms again that both the N-3TH and 4TH signals come from the true spin accumulation in Si. Moreover, since these values estimated from the 4TH [Fig. 6(b)] and N-3TH signals [Fig. 7(d)] in the lateral device are close to those estimated from the N-3TH signals [Fig. 3(c)] in the vertical device ($P_{3T} = 16\%$ and $\tau_S = 1.7$ ns), it is quite reasonable to conclude that Eqs. (4) and (5) precisely express the spin accumulation signals under the geometrical effects, CCE and EAE. Therefore, these equations are appropriate for accurate estimation of P_{3T}, P_{4T}, and τ_S in lateral device structures.

D. Comparison of the fitting results with and without the geometrical effects

To confirm this conclusion, we fitted the following three sets of equations and parameters (P_{3T}, P_{4T}, τ_S) listed in Table I to the N-3TH signals observed in both the vertical and lateral devices [Figs. 3(c) and 7(d)] and the 4TH signals observed in the both setup I [Fig. 6(b)] and setup II (not shown): (i) Eqs. (4) and (5) (both CCE and EAE are taken into account), (ii) Eqs. (4) and (5) with $l^I, l^D \to 0$ [without EAE, Eqs. (S20) and (S21) in SM [34]], and (iii) Eq. (4) with $\lambda_S/t_{SOI} = 1$ and $l^I, l^D \to 0$ and Eq. (2) [without CCE and EAE, Eq. (3) in Ref. [10]]. The estimated values ($P_{3T} = 16\%$ and $\tau_S = 1.7$ ns) from the N-3TH signals in the vertical device (shown in the second and third columns of Table I) were identical because both the electrode length (17.8 μm) and channel thickness (675 μm) are much larger than $\lambda_S = 1.0\,\mu$m. Also, P_{4T} and τ_S estimated from the 4TH signals with $I = +50$ mA (the spin injection regime) in both setups I and II are listed in Table II. The parameters related to the N-3TH signals are not listed in Table II because they were not clearly observed in the spin injection regime ($I > 0$), probably due to the depletion-layer formation, as mentioned before. Note that the 4TH signal was not detected in setup II with $I = -50$ mA (marked by ND in Table I), although the 4TH signal was observed with both bias polarities in setup I. This probably comes from the

TABLE II. P_{4T} and τ_S estimated from the experimental signals with $I = +50$ mA (spin-injection regime), using Eq. (5) under the same conditions as in Table I.

	Lateral device			
	4TH (setup I)		4TH (setup II)	
Condition	P_{4T} (%)	τ_S (ns)	P_{4T} (%)	τ_S (ns)
(i)	7.5	1.9	12	2.3
(ii)	2.7	2.3	7.2	3.2
(iii)	12	2.3	32	3.2

unwanted electric field concentration [41] at the left edge of electrode B (the side closer to electrode R2), and effective channel length becomes longer than L_{ch}, so that spin-polarized electrons cannot reach the detector electrode (electrode A; see SM [34]).

From the fitting results in Tables I and II, the following features are clarified: (a) For the spin polarization, $P =$ 11–63% is estimated with set (iii), while $P = 2.5$–14% is estimated with set (ii). P values are overestimated without CCE, especially when l^{I} is longer (setup II). (b) For the spin lifetime, $\tau_{\mathrm{S}} = 2.1$–3.2 ns is estimated with set (ii), while $\tau_{\mathrm{S}} = 1.7$–2.3 ns is estimated with set (i). Without EAE, τ_{S} values are overestimated, especially when l^{I} or l^{D} is longer. (c) $P = 2.5$–7.2% is estimated with set (ii), while $P = 7.2$–12% is estimated with set (i) in 4TH. Without EAE, P values in 4TH are underestimated, especially when l^{D} is longer (setup I). (d) With CCE and EAE, variation of the estimated values decreased from $P =$ 11–63% and $\tau_{\mathrm{S}} = 1.0$–3.2 ns (set (iii)) to $P = 6.6$–12% and $\tau_{\mathrm{S}} = 1.3$–2.3 ns (set (i)), and these values are close to those in the vertical device ($P = 16\%$ and $\tau_{\mathrm{S}} = 1.7$ ns). From features (a)–(d), we concluded that both CCE and EAE must be taken into account [using Eqs. (4) and (5)] for the precise analysis of the N-3TH and 4TH signals in the thin channel device structure.

IV. CONCLUSION

First, we investigated magnetotransport properties of Fe/Mg/MgO/Si tunnel junctions (vertical device) with various Mg insertion layer thicknesses t_{Mg} with three-terminal Hanle measurements. The formation of a magnetically dead layer at the Fe/MgO interface was prevented by inserting an ultrathin Mg layer ($t_{\mathrm{Mg}} \geqslant 0.5$ nm) between Fe and MgO. The highest spin polarization $P = 16\%$ was achieved when $t_{\mathrm{Mg}} = 1$ nm. These results are consistent with our previously proposed model, which suggests that a magnetically dead (paramagnetic) layer forming at the ferromagnetic metal/oxide interface causes B-3TH and I-3TH signals and reduces the spin injection polarization. This study experimentally shows the relationship between true spin injection/extraction signals (N-3TH) and other B-3TH and I-3TH signals.

Then, realization of spin injection/extraction and pure spin current was verified by the observation of both the four-terminal spin-valve effect and the four-terminal Hanle effect using the lateral device structure with $t_{\mathrm{Mg}} = 1$ nm. The fitting functions were originally derived from the 2D spin diffusion model, taking into account the geometrical effects, CCE and EAE. Using the fitting functions with the geometrical effects [Eqs. (4) and (5)], the P and spin lifetime τ_{S} values estimated in both the vertical and lateral devices are in good agreement. On the other hand, using the fitting functions without the geometrical effects, they are not in agreement between the vertical devices and lateral devices. These results indicate that the geometrical effects must be taken into account [Eqs. (4) and (5)] for the precise estimation of P and τ_{S}.

To realize spin transistors with highly spin dependent output characteristics, further understanding and control of the spin injection/extraction efficiency are needed. This work provides a universal procedure to analyze the spin injection/detection signals observed in both vertical and lateral devices and will contribute to the precise understanding of the physics concerning spin injection/extraction and spin transport in semiconductor device structures.

ACKNOWLEDGMENTS

This work was partially supported by Grants-in-Aid for Scientific Research, including Specially Promoted Research, CREST of JST, Project for Developing Innovation Systems of MEXT, the Yazaki Science and Technology Foundation, and the Spintronics Research Network of Japan. Part of this work was carried out under the Cooperative Research Project Program of RIEC, Tohoku University.

[1] S. Sugahara and M. Tanaka, Appl. Phys. Lett. **84**, 2307 (2004).
[2] S. Sugahara and M. Tanaka, ACM Trans. Storage **2**, 197 (2006).
[3] M. Tanaka and S. Sugahara, IEEE Trans. Electron Devices **54**, 961 (2007).
[4] R. Nakane, T. Harada, K. Sugiura, and M. Tanaka, Jpn. J. Appl. Phys. **49**, 113001 (2010).
[5] T. Tahara, H. Koike, M. Kameno, S. Sasaki, Y. Ando, K. Tanaka, S. Miwa, Y. Suzuki, and M. Shiraishi, Appl. Phys. Express **8**, 113004 (2015).
[6] B. Huang, D. J. Monsma, and I. Appelbaum, Phys. Rev. Lett. **99**, 177209 (2007).
[7] H.-J. Jang and I. Appelbaum, Phys. Rev. Lett. **103**, 117202 (2009).
[8] T. Sasaki, T. Oikawa, M. Shiraishi, Y. Suzuki, and K. Noguchi, Appl. Phys. Lett. **98**, 012508 (2011).
[9] M. Kameno, Y. Ando, T. Shinjo, H. Koike, T. Sasaki, T. Oikawa, T. Suzuki, and M. Shiraishi, Appl. Phys. Lett. **104**, 092409 (2016).
[10] T. Sasaki, T. Oikawa, T. Suzuki, M. Shiraishi, Y. Suzuki, and K. Noguchi, IEEE Trans. Magn. **46**, 1436 (2010).
[11] Y. Saito, M. Ishikawa, H. Sugiyama, T. Inokuchi, K. Hamaya, and N. Tezuka, J. Appl. Phys. **117**, 17C707 (2015).
[12] A. Fert and H. Jaffrès, Phys. Rev. B **64**, 184420 (2001).
[13] Y. Takamura, T. Akushichi, A. Sadano, T. Okishio, Y. Shuto, and S. Sugahara, J. Appl. Phys. **115**, 17C307 (2014).
[14] Y. Takamura, T. Akushichi, Y. Shuto and S. Sugahara, J. Appl. Phys. **117**, 17D919 (2015).
[15] J. Thinga and J.-S. Wang, J. Appl. Phys. **109**, 124303 (2011).
[16] A. Tiwari, T. Inokuchi, M. Ishikawa, H. Sugiyama, N. Tezuka, and Y. Saito, Jpn. J. Appl. Phys. **56**, 04CD05 (2017).
[17] Y. Aoki, M. Kameno, Y. Ando, E. Shikoh, Y. Suzuki, T. Shinjo, M. Shiraishi, T. Sasaki, T. Oikawa, and T. Suzuki, Phys. Rev. B **86**, 081201 (2012).
[18] O. Txoperena, M. Gobbi, A. Bedoya-Pint, F. Golmar, X. Sun, L. E. Hueso, and F. Casanova, Appl. Phys. Lett. **102**, 192406 (2013).
[19] O. Txoperena, Y. Song, L. Qing, M. Gobbi, L. E. Hueso, H. Dery, and F. Casanova, Phys. Rev. Lett. **113**, 146601 (2014).
[20] Y. Song and H. Dery, Phys. Rev. Lett. **113**, 047205 (2014).

[21] S. Sato, R. Nakane, and M. Tanaka, Appl. Phys. Lett. **107**, 032407 (2015).
[22] X. Lou, C. Adelmann, M. Furis, S. A. Crooker, C. J. Palmstrøm, and P. A. Crowell, Phys. Rev. Lett. **96**, 176603 (2006).
[23] T. Linn and D. Mauri, US Patent No. 6841395 (2005).
[24] F. J. Jedema, H. B. Heersche, A. T. Filip, J. J. A. Baselmans, and B. J. Van Wees, Nature (London) **416**, 713 (2002).
[25] T. Shinjo, N. Hosoito, K. Kawaguchi, N. Nakayama, T. Takada, and Y. Endoh, J. Magn. Magn. Mater. **54**, 737 (1986).
[26] S. G. Wang, G. Han, G. H. Yu, Y. Jiang, C. Wang, A. Kohn, and R. C. C. Ward, J. Magn. Magn. Mater. **310**, 1935 (2007).
[27] G. Simmons, J. Appl. Phys. **34**, 1793 (1963).
[28] D. R. Lide, *CRC Handbook of Chemistry and Physics*, 84th ed. (CRC Press, Boca Raton, FL, 2003).
[29] S. P. Dash, S. Sharma, J. C. Le Breton, J. Peiro, H. Jaffrès, J.-M. George, A. Lemaître, and R. Jansen, Phys. Rev. B **84**, 054410 (2011).
[30] M. Kameno, Y. Ando, E. Shikoh, T. Shinjo, T. Sasaki, T. Oikawa, Y. Suzuki, T. Suzuki, and M. Shiraishi, Appl. Phys. Lett. **101**, 122413 (2012).
[31] Y. Ando, K. Kasahara, K. Yamane, Y. Baba, Y. Maeda, Y. Hoshi, K. Sawano, M. Miyao, and K. Hamaya, Appl. Phys. Lett. **99**, 012113 (2011).
[32] Z. G. Yu and M. E. Flatté, Phys. Rev. B **66**, 235302 (2002).
[33] J. Suñé, P. Olivo, and B. Riccó, J. Appl. Phys. **70**, 337 (1998).
[34] See Supplemental Material at http://link.aps.org/supplemental/10.1103/PhysRevB.96.235204 for (S1) derivation of the three-dimentional impulse response for the vertical device, (S2) derivation of the two-dimentional impulse response for the vertical device, (S3) derivation of the 2D impulse response for the lateral device, (S4) three-terminal Hanle signals in a vertical device structure, (S5) three-terminal and four-terminal Hanle signals in the lateral device, (S6) bias dependence of N-3TH signals in degenerated semiconductors, and (S7) the reason for the absence of four-terminal Hanle signals in setup II.
[35] *Optical Orientation*, edited by B. P. Zakharchenya and F. Mayer (Elsevier, Amsterdam, 1984).
[36] R. J. Soulen, Jr., J. M. Byers, M. S. Osofsky, B. Nadgorny, T. Ambrose, S. F. Cheng, P. R. Broussard, C. T. Tanaka, J. Nowark, J. S. Moodera, A. Barry, and J. M. D. Coey, Science **282**, 85 (1998).
[37] R. Jansen, S. P. Dash, S. Sharma, and B. C. Min, Semicond. Sci. Technol. **27**, 083001 (2012).
[38] O. Txoperena and F. Casanova, J. Phys. D **49**, 133001 (2016).
[39] Y. Song, O. Castner, and H. Dery, Phys. Rev. Lett. **113**, 167201 (2014).
[40] S. Sharma, S. P. Dash, H. Saito, S. Yuasa, B. J. van Wees, and R. Jansen, Phys. Rev. B **86**, 165308 (2012).
[41] R. Nakane, S. Sato, S. Kokutani, and M. Tanaka, IEEE Magn. Lett. **3**, 3000404 (2012).